

# Winds from clusters with non-uniform stellar distributions

Rodríguez-González, A.<sup>1</sup> \*; Cantó, J.<sup>2</sup>; Esquivel, A.<sup>1</sup>, Raga, A. C.<sup>1</sup> & Velazquez, P. F.<sup>1</sup>

<sup>1</sup>*Instituto de Ciencias Nucleares, Universidad Nacional Autónoma de México, Apdo. Postal 70-543, 04510, México, D.F., México.*

<sup>2</sup>*Instituto de Astronomía, Universidad Nacional Autónoma de México, Apdo. Postal 70-264, 04510, México, D.F., México.*

Draft Version, 29 October 2018

## ABSTRACT

We present analytic and numerical models of the ‘cluster wind’ resulting from the multiple interactions of the winds ejected by the stars of a dense cluster of massive stars. We consider the case in which the distribution of stars (i. e., the number of stars per unit volume) within the cluster is spherically symmetric, has a power-law radial dependence, and drops discontinuously to zero at the outer radius of the cluster. We carry out comparisons between an analytic model (in which the stars are considered in terms of a spatially continuous injection of mass and energy) and 3D gasdynamic simulations (in which we include 100 stars with identical winds, located in 3D space by statistically sampling the stellar distribution function). From the analytic model, we find that for stellar distributions with steep enough radial dependencies the cluster wind flow develops a very high central density and a non-zero central velocity, and for steeper dependencies it becomes fully supersonic throughout the volume of the cluster (these properties are partially reproduced by the 3D numerical simulations). Therefore, the wind solutions obtained for stratified clusters can differ dramatically from the case of a homogeneous stellar distribution (which produces a cluster wind with zero central velocity, and a fully subsonic flow within the cluster radius). Finally, from our numerical simulations we compute predictions of X-ray emission maps and luminosities, which can be directly compared with observations of cluster wind flows.

**Key words:** Hydrodynamics – shock waves – stars: winds, outflows

## 1 INTRODUCTION

Super star clusters (SSCs) are dense clusters of young massive stars, first identified in NGC 1705 by Melnick et al. (1985) and in NGC 1569 by Arp & Sandage (1985). Recently, they have been observed in a wide range of star-forming galaxies, such as merging systems (NGC 4038/4039, Whitmore & Schweizer 1995), dwarf galaxies (Henize 2-10, Johnson et al. 2000), classical starbursts (M82, Gallagher & Smith 1999, Melo et al. 2005), as well as in our galaxy (Arches Cluster : Nagata et al. 1995; Cotera et al. 1996; Serabyn, Shupe & Figer 1998) amongst many other systems (for a review see Whitmore 2000).

These star clusters can contain hundreds or thousands of very young, energetic stars, and have stellar densities far greater than those seen in normal OB associations. The ages of most of these star clusters are around 1- 10 Myr, their radii typically in the range of  $\sim 1$  -10 pc, and their total cluster masses in the  $10^3$  -  $10^6 M_{\odot}$  range (Melo et al. 2005 reported a mean mass per star cluster, of  $\sim 2 \times 10^5 M_{\odot}$ , for M82). The central stellar densities of SSCs reach up to  $\sim 10^5 M_{\odot} \text{ pc}^{-3}$ . However, we can find SSCs with older ages

and/or larger masses (Walcher et al. 2006 reports a cluster with  $6 \times 10^7 M_{\odot}$ ).

Cantó et al. (2000, hereafter Paper I) explored an analytic model using the physical properties of the *Arches Cluster*. This cluster has  $\sim 100$  massive stars within a  $\sim 0.2$  -  $0.3$  pc radius. Such SSC must have strong multiple stellar wind interactions, resulting in the formation of stellar wind shocks. In Paper I, the cluster wind was modeled as a mass-loading process (Hartquist et al. 1986; Dyson 1992; Lizano et al. 1996), resulting in essentially the same model as the one presented by Chevalier & Clegg (1985, who studied the flow resulting from a continuous temporal and spatial distribution of supernovae explosions).

Both in the stationary solution for spherically symmetric winds (Chevalier & Clegg 1985, Cantó et al. 2000) and in the numerical calculations of Raga et al. (2001) the stellar distribution (within the cluster) was assumed to be homogeneous. Also, these models are adiabatic (or, more precisely, non-radiative) solutions, which are appropriate for SSCs with low to intermediate mass and/or terminal velocity of SSCs (masses around  $10^4$  -  $10^6 M_{\odot}$  and terminal velocities of  $\sim 1000$  km/s). For more massive stellar clusters, lower stellar wind terminal velocities or higher metallicities, radiative

\* ary@nucleares.unam.mx

losses within the cluster wind may become important (see Silich et al. 2004).

In the present paper, we explore a non-radiative analytic model for cluster winds, considering a non-homogeneous stellar distribution (within the cluster). In particular, we study the case in which the stars have a  $n(R) \propto R^\alpha$  power-law distribution (where  $n$  is the number of stars per unit volume as a function of the spherical radius  $R$ ), with  $-3 < \alpha \leq 0$ . We also compute 3D gasdynamical simulations for stellar distribution functions with different values of  $\alpha$ , and compare the properties of the computed flows with the analytic model. This work is a natural extension of the model presented in Paper I.

We note that Matvienko & Shchekinov (2005) have presented a study of mass loaded flows with sources and sinks with power law spatial distributions. The analytic model that we discuss in the present paper is based on a similar set of equations, but describes a cluster wind, rather than a mass loaded stellar wind (as was studied by Matvienko & Shchekinov 2005). Also relevant in the context of the present work are the papers of Raga et al. (2001) and Rockefeller et al. (2005), who carried out 3D numerical simulations of winds from stratified clusters.

The paper is organized as follows. In section 2, we present the analytical solution. In section 3, we describe the numerical simulations and compare the results with the analytic model. Predictions of the X-ray emission from the simulated flows are described in section 4. Finally, we summarize our results in section 5.

## 2 THE ANALYTIC MODEL

We consider  $N$  identical stars in a spherical cluster with an outer radius  $R_c$ . The stars have a spatial distribution (number of stars per unit volume) of the form,

$$n(R) = k_c R^\alpha = \frac{(3 + \alpha)N}{4\pi R_c^{3+\alpha}} R^\alpha, \quad (1)$$

where  $R$  is the spherical radius,  $\alpha$  and  $k_c$  are constants. In the second equality, the constant  $k_c$  has been computed using the normalization condition

$$\int_0^{R_c} 4\pi R^2 n(R) dR = N. \quad (2)$$

Every star has an identical wind with mass and energy deposition rates  $\dot{M}_w$  and  $\dot{E}_w$ , respectively, and terminal velocity  $V_w$ . For highly supersonic wind,  $\dot{E}_w = \frac{1}{2}\dot{M}_w V_w^2$ . The stellar winds are thermalized at shocks (produced by interactions between the multiple winds), resulting in the production of a hot intercluster gas. This gas has a large central overpressure, which eventually produce a stationary ‘cluster wind’ flow.

For an adiabatic, spherically symmetric cluster wind (and neglecting the gravity due to the stellar distribution), the mass, momentum and energy equations are :

$$\frac{1}{R^2} \frac{d}{dR} (\rho V R^2) = n(R) \dot{M}_w, \quad (3)$$

$$\rho V \frac{dV}{dR} = -\frac{dP}{dR} - n(R) \dot{M}_w V, \quad (4)$$

$$\frac{1}{R^2} \frac{d}{dR} \left[ \rho V R^2 \left( \frac{V^2}{2} + h \right) \right] = n(R) \dot{E}_w, \quad (5)$$

$\rho$  and  $V$  are the mass density and velocity of the wind respectively,  $R$  is the radial coordinate,

$$h = \frac{\gamma}{\gamma - 1} \frac{P}{\rho}, \quad (6)$$

and  $h$  is the specific enthalpy,  $P$  is the mean gas pressure and  $\gamma$  is the specific heat ratio.

Equation (3) implies that

$$\rho V = \frac{\dot{M}_c}{4\pi R_c^{3+\alpha}} R^{1+\alpha}, \quad (7)$$

where  $\dot{M}_c \equiv N\dot{M}_w$  is the total mass loss rate from the cluster in steady state. This equation shows that the mass flux profile strongly depends on the  $\alpha$  exponent.

The adiabatic sound speed  $c_s$  is given by,

$$c_s^2 = \gamma \frac{P}{\rho} = \gamma \frac{kT}{\mu}, \quad (8)$$

where  $T$  is the gas temperature,  $\mu$  is the mean mass per particle and  $k$  is the Boltzmann constant. Integrating equation (5) and using equations (6) and (8) we find

$$c_s^2 = \frac{\gamma - 1}{2} (V_w^2 - V^2). \quad (9)$$

Now, combining equations (4), (7) and (9) we obtain

$$\frac{1 - cv^2}{a + bv^2} \frac{dv^2}{v^2} = \frac{dr^2}{r^2}, \quad (10)$$

where,  $a = 1 + \alpha$ ,  $b = (1 + \alpha + [5 + \alpha]\gamma)/(\gamma - 1)$ , and  $c = (\gamma + 1)/(\gamma - 1)$ . In terms of the dimensionless variables,  $v = V/V_w$   $r = R/R_c$ , this equation admits solutions,

$$v^p (a + bv^2)^q = Ar \quad v = (-a/b)^{1/2} = const. \quad (11)$$

In equation (11),  $p = 1/a$ ,  $q = -(b + ac)/(2ab)$  and  $A$  is an integration constant.

Outside the cluster (i. e., for  $R > R_c$ )  $n(R) = 0$ , and the mass and momentum conservation equations have the form,

$$\frac{1}{R^2} \frac{d}{dR} (\rho V R^2) = 0, \quad (12)$$

$$\rho V \frac{dV}{dR} = -\frac{dP}{dR}. \quad (13)$$

Combining equations (12) and (13), we obtain,

$$v (1 - v^2)^{1/(\gamma-1)} = \frac{B}{r^2}, \quad (14)$$

where,  $B$  is a constant.

The velocity of the flow, ( $v_1$ ) at the outer boundary of the cluster ( $r = R/R_c = 1$ ) follows from equation (14),

$$v_1 (1 - v_1^2)^{1/(\gamma-1)} = B. \quad (15)$$

The value of the integration constants  $A$  and  $B$  are determined by the boundary conditions at  $r = 1$  ( $R = R_c$ ) and  $r \rightarrow \infty$ . They, of course, depend also on the value of  $\alpha$ . There are three different regimes :

a.  $\alpha \geq -1$  :

In this regime,  $p > 0$  and  $q < 0$  (also both  $a$  and  $b > 0$ ). From equation (11) we can see that very close to the centre of the cluster,

$$v \sim (Ar)^{1/p}. \quad (16)$$

The wind velocity inside the cluster is subsonic, the velocity at the centre of the cluster is zero and the density is finite. The gas velocity increases towards the outer cluster boundary, and the flow at this boundary ( $r = 1$ ) follows from equation (11),

$$A = v_1^p [a + bv_1^2]^q. \quad (17)$$

The left-hand side of equation (15) has a maximum value of

$$\left(\frac{\gamma-1}{\gamma+1}\right)^{1/2} \left(\frac{2}{\gamma+1}\right)^{1/(\gamma-1)}, \quad (18)$$

for  $v_1 = [(\gamma-1)/(\gamma+1)]^{1/2}$ . The requirement that the pressure at infinity must go to zero implies that the flow has to adopt the critical solution, for which

$$A = \left(\frac{\gamma-1}{\gamma+1}\right)^{p/2} \left(a + b\frac{\gamma-1}{\gamma+1}\right)^q, \quad (19)$$

and,

$$B = \left(\frac{\gamma-1}{\gamma+1}\right)^{1/2} \left(\frac{2}{\gamma+1}\right)^{1/(\gamma-1)} \quad (20)$$

We can then use equations (7), (8), (9) and (16) to obtain the properties of the cluster wind at the centre of the cluster (see Paper I):

$$\rho_0 = \frac{\dot{M}_c}{4\pi A^a R_c^2 V_w}, \quad (21)$$

$$P_0 = \frac{\gamma-1}{2\gamma} \frac{\dot{M}_c V_w}{4\pi A^a R_c^2}, \quad (22)$$

$$T_0 = \frac{\gamma-1}{2\gamma} \frac{\mu}{k} V_w^2. \quad (23)$$

b.  $\alpha_{min} \equiv -\frac{3\gamma+1}{\gamma+1} < \alpha \leq -1$  :

In this interval,  $p < 0$ ,  $q > 0$ ,  $a < 0$  and  $b > 0$ . Thus the velocity inside the cluster is subsonic and has a non-zero value at the cluster centre ( $r = 0$ ). From equation (11)

$$v_0 = \sqrt{-\frac{a}{b}}. \quad (24)$$

On the other hand, equation (7) indicates that the mass flux of the wind is inversely proportional to a positive power of  $r$ . This implies that the central gas density tend to infinite. From equations (8), (9) and (24) the central temperature is,

$$T_0 = \frac{\gamma-1}{2\gamma} \frac{\mu}{k} \left(1 + \frac{a}{b}\right) V_w^2. \quad (25)$$

c.  $\alpha_{cr} \equiv -3 < \alpha \leq \alpha_{min}$ :

In this regime,  $p > 0$ ,  $q < 0$ ,  $a < 0$  and  $b > 0$ , the velocity of the wind remains constant (with a supersonic value) within the cluster. Its magnitude is given by equation (24). The temperature is also uniform inside the cluster and is given by equation (25). The density also goes to infinity at the centre of the cluster and decreases outwards. But the

wind escapes from the cluster surface supersonically, and accelerates outwards, until it reaches the terminal velocity.

We do not consider power-law stellar distributions with  $\alpha < \alpha_{cr} (= -3)$  because they have an infinite number of stars (resulting from the strong divergence of the distribution function in the cluster centre).

### 3 THE NUMERICAL SIMULATIONS

#### 3.1 Numerical setup

In order to illustrate the analytic star cluster wind solutions we have computed 3D numerical simulations with the full, non-radiative gasdynamic equations. The simulations solve a multiple stellar wind interaction problem with the 3D, adaptive grid ‘‘yguazú-a’’ code, which is described in detail by Raga et al. (2000, 2002). The simulations were computed on a five-level binary adaptive grid with a maximum resolution of 0.1172 pc (corresponding to  $256^3$  grid points at the maximum grid resolution) in a computational domain of 30 pc (along each of the 3 coordinate axes).

In all runs, we assumed that the computational domain was initially filled by a homogeneous, stationary ambient medium with temperature  $T_{env} = 500$  K and density  $n_{env} = 0.1 \text{ cm}^{-3}$ . The stellar winds are imposed in spheres (centred at the stellar positions, see below) of radius  $R_w = 2.2 \times 10^{18}$  cm, corresponding to 6 pixels at the maximum resolution of the adaptive grid. Within these spheres, we impose (at all times) a  $T_w = 15000$  K temperature, and an outwardly directed  $V_w = 1000 \text{ km s}^{-1}$  velocity. The density within the spheres has an  $r^{-2}$  law (where  $r$  is the radial coordinate measured outwards from the stellar position), scaled so that the mass loss rate is  $\dot{M}_w = 10^{-5} M_\odot \text{ yr}^{-1}$  for each star. We then place 100 such stellar wind sources within a spherical cluster of outer radius  $R_c = 10$  pc, centred in the computational domain.

We have computed four simulations of clusters with power-law stellar distributions (see equation 1) with  $\alpha = 0, -0.5, -2.0$  and  $-2.5$ . The stellar positions are chosen by statistically sampling the distribution functions in the way described in section 3.2.

#### 3.2 Sampling the stellar position distribution function

In order to produce models that can be compared with the analytic solutions, we place stars within the cluster with positions obtained by randomly sampling the power-law distribution function given by equation (1). This is done as follows.

We first note that  $f(R)dR = C 4\pi R^2 n(R)dR$  (with  $n(R)$  given by equation 1) is the fraction of the stars which have radial positions between  $R$  and  $R + dR$ . Using the normalization condition  $\int_0^{R_c} f(R)dR = 1$ , we obtain

$$f(R) = \left(\frac{3+\alpha}{R_c^{3+\alpha}}\right) R^{2+\alpha}. \quad (26)$$

This normalization is of course valid only for  $\alpha > -3$  since otherwise a divergence occurs at the lower limit of the normalization integral.

With a random number generator we then choose a number  $\eta$  which is uniformly distributed in the interval  $[0, 1]$ . This variable is statistically related to the radius  $R$  through the relation :

$$\int_0^R f(R)dR = \int_0^\eta d\eta. \quad (27)$$

From equations (26-27) we obtain

$$R = R_c \eta^{1/(3+\alpha)} \quad (28)$$

from which we can sample  $R$  as a function of the random number  $\eta$ .

Once we have chosen the radial coordinate for each of the  $N$  stars (used in the simulation) by sampling the radial distribution function (as described above), we assign random directions to the vector position of each of the stars. In this way, we obtain statistical samplings of the stellar position functions.

In practice, we have to modify the obtained stellar distributions because we impose the stellar wind conditions in spheres of a finite radius  $r_w$  (see section 2.1). Whenever we obtain pairs of stellar positions resulting in overlapping “stellar wind spheres”, we eliminate one of the two stars. This leads to an undersampling of the desired distribution function in the central, high stellar density regions of the generated clusters. Because of this, the comparison between the numerical simulations and the analytic cluster wind solutions is only meaningful away from the central region of the cluster.

We should note that the 100 stars of each model were chosen with the same set of random numbers, so that the directions from the cluster centre to each of the stars are the same in all models. However, the physical radii corresponding to the “radial random numbers” differ for each model, as the “conversion” from random number ( $\eta$ ) to physical radius  $R$  (see equation 28) depends on the value of  $\alpha$ .

### 3.3 Model results

We computed four numerical simulations of clusters with stellar distributions with different  $\alpha$  values. All models are computed for clusters with 100 stars and a 10 pc outer radius. The stars are identical, with a mass deposition rate of  $10^{-5} M_\odot \text{ yr}^{-1}$  and a wind velocity of 1000 km/s.

The only difference between the models are the stellar density distributions. We have chosen  $\alpha$  values (see equation 1) covering the different regimes of the cluster wind flow (see section 2).

We have integrated forward in time the four models until stationary flows are obtained. From the stationary flow configurations, we then compute (through appropriate interpolations in the cartesian adaptive grid) the radially dependent flow density, velocity and temperature averaged over spherical concentric surfaces  $S_R = 4\pi R^2$  :

$$\rho_a(R) = \frac{1}{4\pi} \int_{S_R} \rho \sin \theta d\theta d\phi, \quad (29)$$

$$v_a(R) = \frac{1}{4\pi\rho_a(R)} \int_{S_R} \rho v_R \sin \theta d\theta d\phi, \quad (30)$$

$$T_a(R) = \frac{1}{4\pi\rho_a(R)} \int_{S_R} \rho T \sin \theta d\theta d\phi, \quad (31)$$

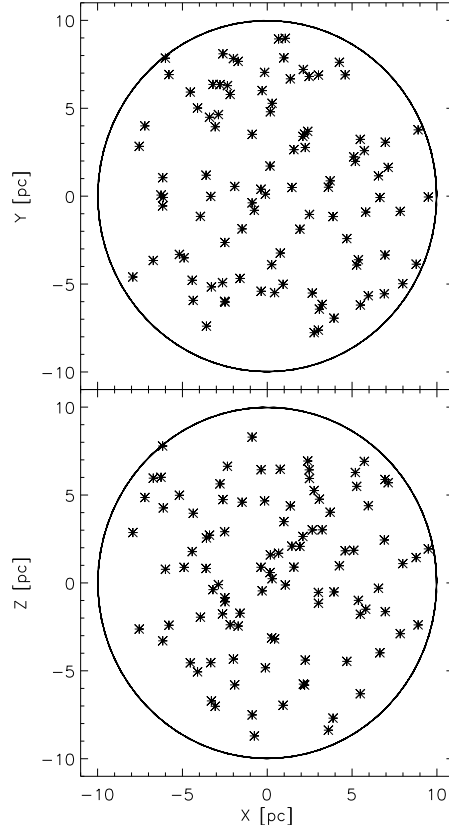


**Figure 1.** The stellar distribution of xy-plane and xz-plane for the  $\alpha = 0$  model. The solid line represents the outer boundary of the cluster.

where  $\theta$  and  $\phi$  are the polar and azimuthal angles, respectively, and  $\rho$  is the flow density,  $T$  the temperature and  $v_R$  the radial velocity (obtained by projecting the three cartesian velocity components resulting from the numerical integration onto the direction normal to the spherical surface). That is  $v_R = (xv_x + yv_y + zv_z)/R$ . We then compare this spherically averaged flow with the results from our analytic cluster wind model.

#### 3.3.1 The $\alpha \geq -1$ case

For this  $\alpha$  range we ran two models: a cluster with a homogeneous (i.e.,  $\alpha = 0$ ) stellar density distribution, and a cluster with an  $\alpha = -0.5$  distribution.

The stellar distribution used for the  $\alpha = 0$  model (obtained by sampling the  $\alpha = 0$  distribution function, see equation 26 and section 3.2) is shown in Figure 1. The average flow variables as a function of spherical radius (obtained by averaging over concentric spherical shells, see above) are compared with the solution obtained from the analytic model in Figure 2. From this Figure, it is clear that the average density, velocity and temperature (obtained from the numerical simulation) agree very well with the analytical model, except close to the centre of the cluster. The deviations in the cluster centre are a direct result of the small

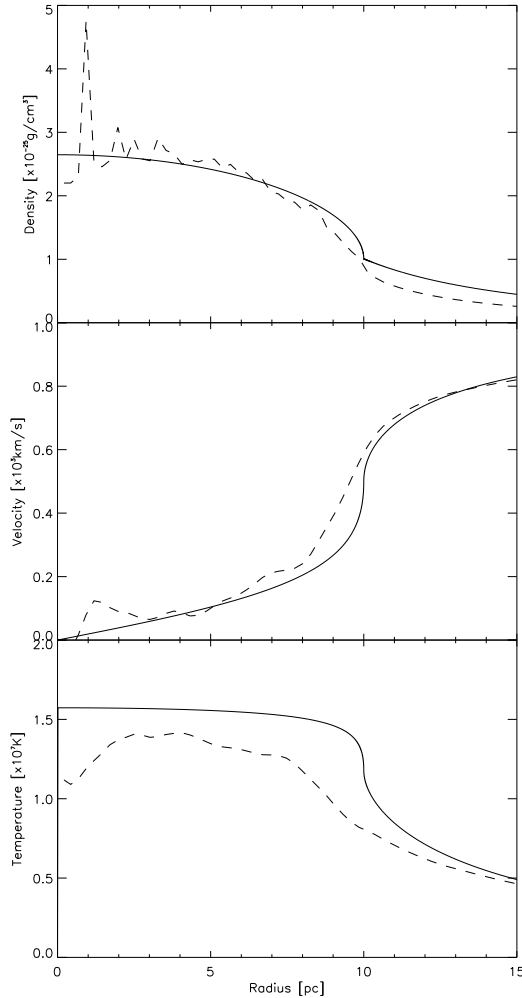


**Figure 2.** The spherically averaged flow obtained from the  $\alpha = 0$  model. The density (top), radial velocity (centre) and temperature (bottom) obtained from the numerical simulations (dashed lines) and the analytic model (solid lines) are shown as a function of spherical radius  $R$ .

number of stars that is present within the inner  $\sim 3$  pc of the cluster (see Figure 1).

Figure 3 illustrates the real complexity of the flow that is obtained from the numerical simulations. This Figure shows a 3D rendition of the 10 pc radius star cluster, with 100 stars and  $\alpha = 0$ . The flow has a sponge-like morphology, with low density stellar wind cavities immersed in the denser ‘cluster wind’ flow (composed of shocked stellar wind material). The relatively monotonic average flow (shown in Figure 2) is obtained by averaging over this complex flow structure.

The stellar distribution used for the  $\alpha = -0.5$  model (obtained by sampling the  $\alpha = -0.5$  distribution function, see equation 26 and section 3.2) is shown in Figure 4. The average flow variables as a function of spherical radius (obtained by averaging over spherical surfaces, see above) are compared with the solution obtained from the analytic model in Figure 5. Again, a reasonably good agreement is obtained between the analytic model and the average flow

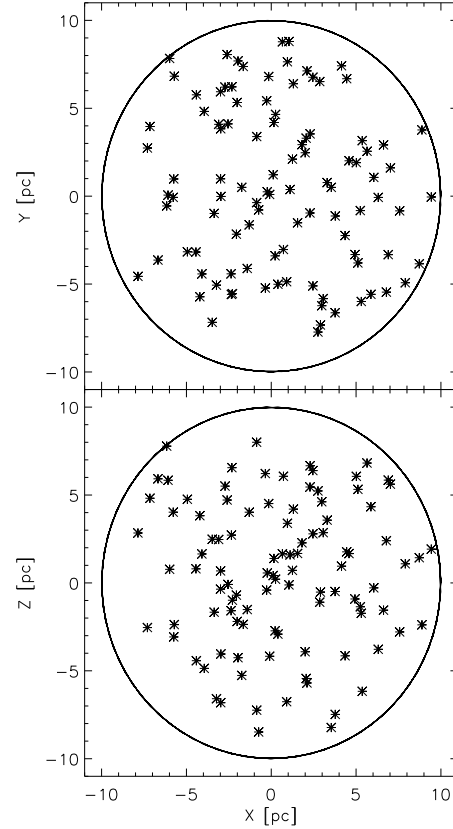


**Figure 4.** Same as Figure 1, but for the  $\alpha = -0.5$  model.

variables computed from the flow that results from the numerical simulation, except for the inner region of the cluster.

### 3.3.2 The $\alpha_{min} < \alpha < \alpha_c$ case

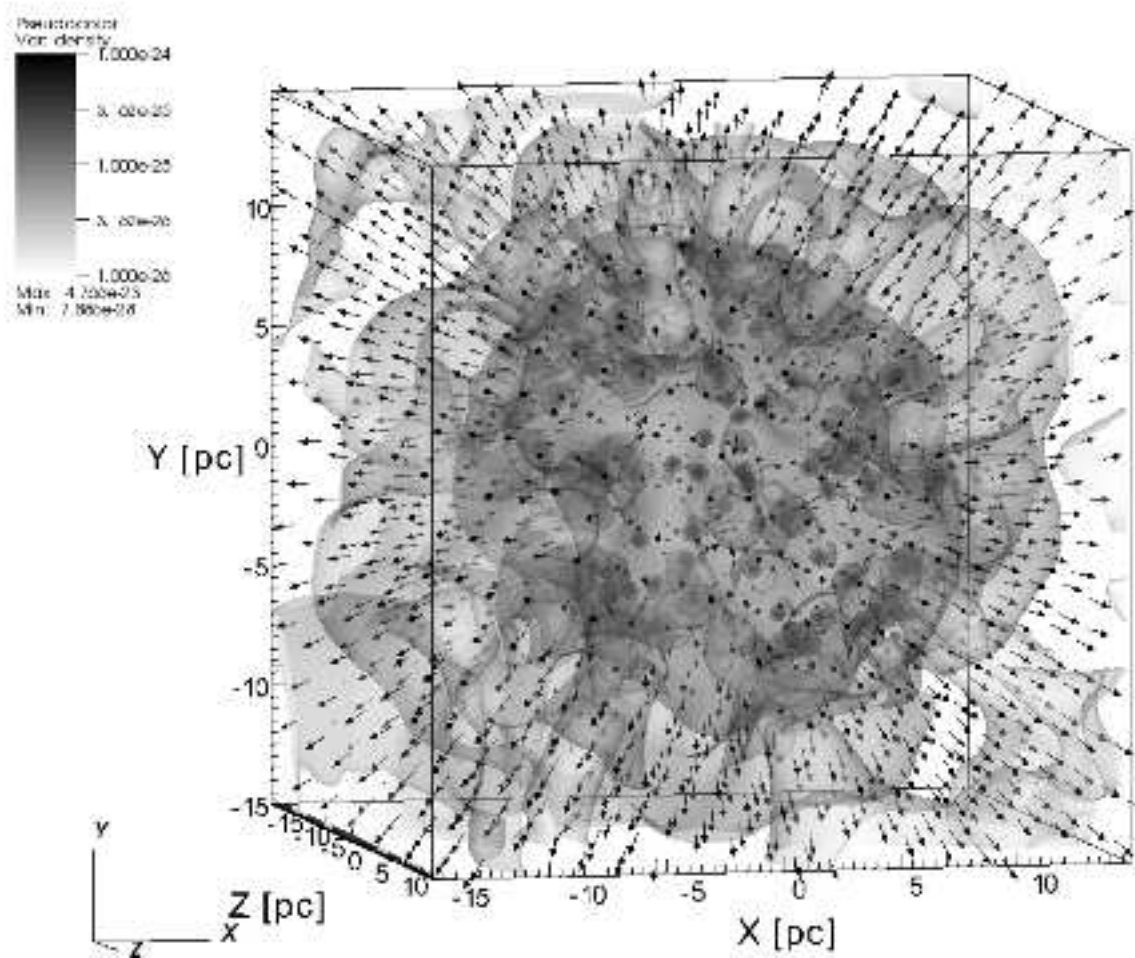
Figure 6 shows the stellar positions that results from sampling the  $\alpha = -2$  distribution function. The stars are highly concentrated around the centre of the cluster.

Figure 7 shows the angularly averaged velocity, density and temperature as a function of the radial coordinate. The analytical solution has a non-zero, subsonic velocity and an infinite density at the central position of the cluster.

Substantial differences between the numerical and analytical solutions are found for radii smaller than  $\sim 4$  pc. This is a direct result of the undersampling of the stellar distribution function which occurs as a result of the ‘proximity criterion’ (described in 3.2) applied for placing the stars in the computational grid. For larger radii, a reasonable agreement between the analytical and numerical results is obtained.

### 3.3.3 The $\alpha_{cr} < \alpha < \alpha_{min}$ case

Figure 8 shows the stellar positions that results from sampling the  $\alpha = -2.5$  distribution function. The analytical solution and the angularly average flow variables (obtained from the numerical simulation) are shown in Figure 9. For



**Figure 3.** 3D rendition of the model with 100 stars distributed homogeneously ( $\alpha = 0$ ) inside of a sphere of 10 pc in radius. In logarithmic grey-scale (colour-scale in the online version) we present 5 isosurfaces of density. Depicted by arrows we overlaid the velocity field, the largest arrow corresponds to a magnitude of  $10^3 \text{ km s}^{-1}$ .

this model, the analytic solution has a supersonic, outwards velocity in the inner region of the cluster. Again we obtain substantial deviations between the analytic and numerical solutions in the central region of the cluster, and better agreement for larger radii.

#### 4 PREDICTED X-RAY EMISSION

We have taken the density and temperature stratifications for the steady cluster wind flow configurations, and used them to compute the X-ray emission. We have done this by computing the emission coefficient in the  $0.3 \rightarrow 2 \text{ keV}$  photon energy range using the CHIANTI<sup>1</sup> atomic data base and software (see Dere et al. 2001 and references therein).

<sup>1</sup> The CHIANTI database and associated IDL procedures, now distributed as version 3.0, are freely available at the following addresses on the World Wide Web: <http://www.solar.nrl.navy.mil/chianti.html>,

For this calculation, it is assumed that the ionisation state of the gas corresponds to coronal ionisation equilibrium, and that the emission is in the low density regime (i. e., that the emission coefficient is proportional to the square of the density).

We then integrate this emission coefficient along lines of sight, which are assumed to be parallel to the  $y$ -axis of the computational grid. The X-ray maps computed in this way for the models with  $\alpha = 0, -0.5, -2$  and  $-2.5$  are shown in Fig. 10.

From these maps, it is clear that the X-ray emission is highly structured in all models. Actually, some of the structures are seen in all four models, as the stellar position have been chosen with the same set of random numbers (but not the same radial positions, see the discussion at the end of §3.2).

In Figure 11, we show the emission along a line of sight

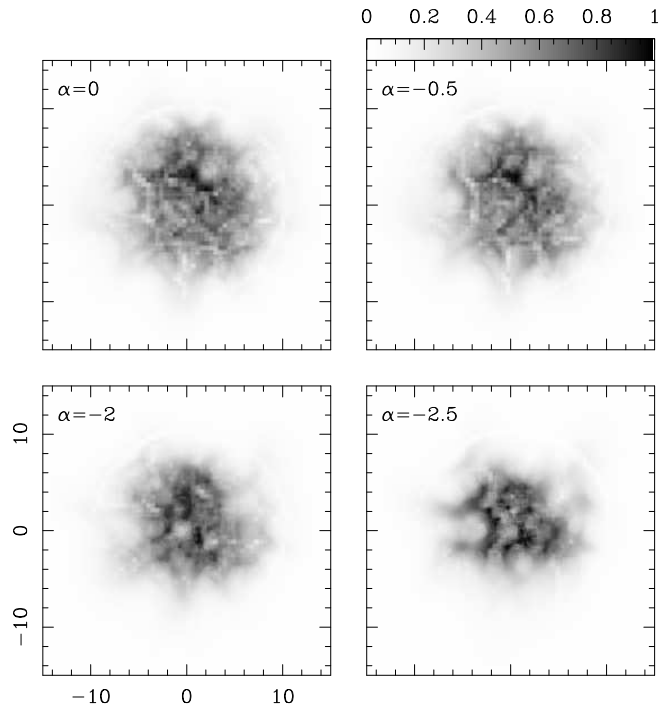


**Figure 10.** X-ray images obtained by integrating the emission coefficient along lines of sight (parallel to  $z$ -axis) and over energies ranging from 0.3 to 2 keV, for the four models described in the text. The images are depicted with gray scale (with the fluxes normalized to the maximum value) given by the bar to the top of the right-top plot). The scales along the  $x$ - and  $y$ -axes are given in units of parsecs, with the origin coinciding with the barycenter of the stellar distribution of the cluster.

placed at  $x, y=0$  four X-ray maps of Figure 10. These cuts show that the  $\alpha = 0$  and  $\alpha = -0.5$  models have a structured but more or less constant emission within a radius of  $\sim 6$  pc (i. e., the inner 60 % of the cluster radius), with wings of lower emission extending to beyond the outer cluster boundary. The models with steeper stellar distribution functions (i. e., with more negative values of  $\alpha$ ) show more compact emission structures.

Finally, by integrating the X-ray emission over the whole emitting volume, we compute luminosities of 0.32, 0.32, 0.26 and 0.20  $L_{\odot}$  for the  $\alpha = 0, -0.5, -2$  and  $-2.5$ , respectively. Therefore, we find that while the predicted maps differ quite appreciably between the different models, the X-ray luminosity does not depend strongly on the value of  $\alpha$ .

We should note that because the emission coefficient is proportional to the square of the density, one can use equation (21) to deduce the scaling of the X-ray luminosity

to other model parameters. For example, a supercluster with  $\sim 20000$  stars would have X-ray luminosities of  $\sim 8 \rightarrow 12 \times 10^3 L_{\odot}$  (depending on the value of  $\alpha$ , see above).

## 5 CONCLUSIONS

In this paper we have extended the analytic cluster wind model of Paper I to the case of a non-uniform stellar distribution. In particular, we have studied the case of a radially dependent,  $n(R) = k_c R^{\alpha}$  power-law distribution.

Of particular interest is the  $\alpha = -2$  distribution, which corresponds to the stratification of a singular, isothermal, self-gravitating sphere. Such a structure is of interest for modelling the wind from a gravitationally bound stellar cluster. Power-law stellar distributions with other values of  $\alpha$  do not have a clear physical justification, but can be considered as a parametrization of stellar distributions with different degrees of central condensation.

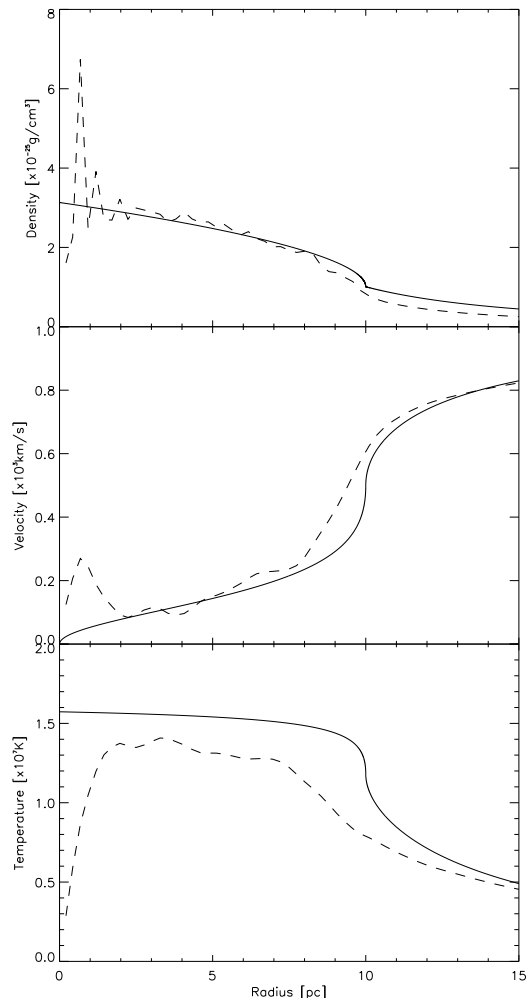


**Figure 5.** Same as Figure 2, but for the  $\alpha = -0.5$  model.

We find that for shallow distributions, with  $-1 < \alpha < 0$ , the cluster wind has zero velocity in the cluster centre. However, for more negative  $\alpha$  values the cluster wind has a non-zero, outwards directed velocity (subsonic for  $\alpha_{min} < \alpha < -1$  and supersonic for  $-3 < \alpha < \alpha_{min}$ ) in the centre of the cluster. The solutions with a non-zero central velocity have an infinite central density for the cluster wind.

We have then compared the analytic cluster wind solutions with 3D numerical simulations. For carrying out the simulations, we consider the winds from 100 stars, with a spatial distribution obtained by statistically sampling the appropriate stellar distribution function. We then carry out angular averages of the computed flow variables, and compare the radial dependence of these averages with the predictions obtained from the analytic model.

For different values of  $\alpha$ , we obtain a good agreement between the analytic and numerical predictions in the outer regions of the cluster. However, the analytic and numerical solutions have large differences in the central region of the cluster. These differences are a direct result of the fact that only a small number of stars are present in this spatially reduced region, and therefore the continuous mass and en-

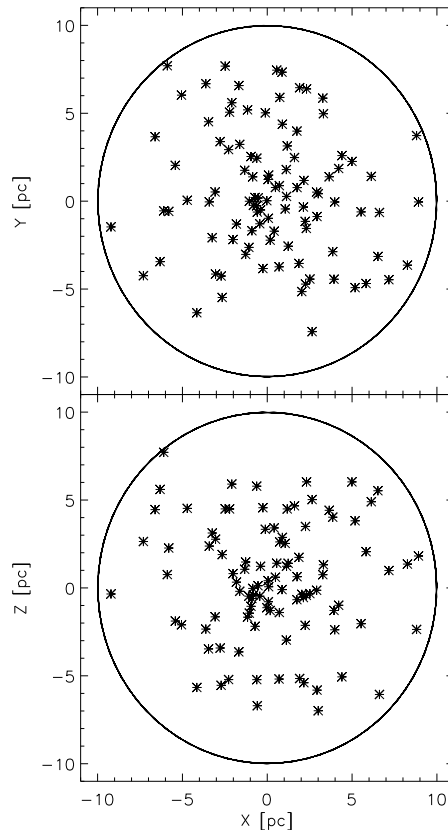


**Figure 6.** Same as Figure 1, but for the  $\alpha = -2$  model.

ergy source distribution assumed in the analytic model is inappropriate for describing the real cluster wind flow.

Finally, we have obtained predictions of the X-ray emission from our simulated cluster wind flows. Our models have quite low  $\sim 0.2 \rightarrow 0.3 L_{\odot}$  X-ray luminosities, as a result of the fact that only 100 stars were included (due to the constraints imposed by the numerical resolution of the simulations). However, the scaling laws of the analytic model imply that models with 20000 stars (i. e., with the number of stars of a large supercluster) will have X-ray luminosities of  $\sim 10^4 L_{\odot}$  (see section 4). At distances of  $\sim 4$  Mpc (i. e., the distance to M 82), this would produce an X-ray flux of  $\approx 2 \times 10^{-14} \text{ erg s}^{-1} \text{ cm}^{-2}$ . Such a flux is only 2 % of the X-ray flux observed for the Arches cluster close to the galactic centre (see Yusef-Zadeh et al. 2002), but might be within range for possible future observations.

An important remaining problem is that  $H\alpha$  emission has been observed from many superclusters. Our models have gas temperatures in excess of  $10^7$  K, and therefore do not produce such an emission. Therefore, the observed  $H\alpha$  emission must be coming from another component, which could be the remnants of dense interstellar clouds which were present in the region when the cluster was formed. The presence of such dense, lower temperature structures within the cluster wind flow could be explored in the future with numerical simulations similar to the ones which we have shown in the present paper, but that need to include the radiative cooling.

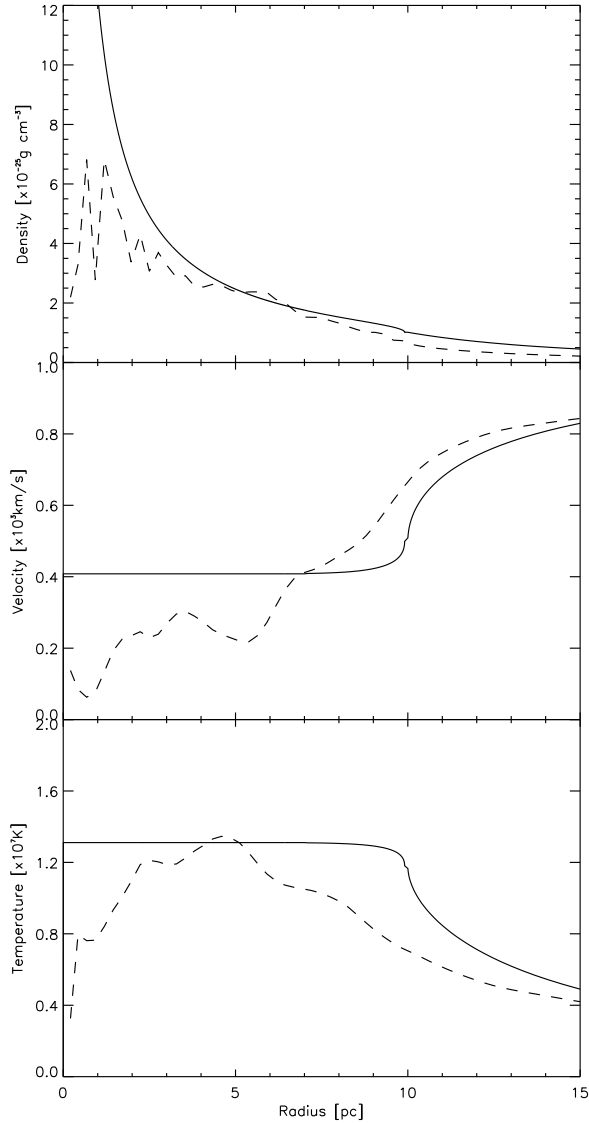


Figure 7. Same as Figure 2 but for the  $\alpha = -2$  model.

## ACKNOWLEDGEMENTS

This work was supported by the CONACyT grant 46828-F, the DGAPA (UNAM) grant IN 108207 and the “Macroproyecto de Tecnologías para la Universidad de la Información y la Computación” (Secretaría de Desarrollo Institucional de la UNAM, Programa Transdisciplinario en Investigación y Desarrollo para Facultades y Escuelas, Unidad de Apoyo a la Investigación en Facultades y Escuelas).

We thank Enrique Palacios and Martín Cruz for supporting the servers in which the calculations of this paper were carried out.

## REFERENCES

rp, H. & Sandage, A., 1985, *AJ*, 90, 1163.

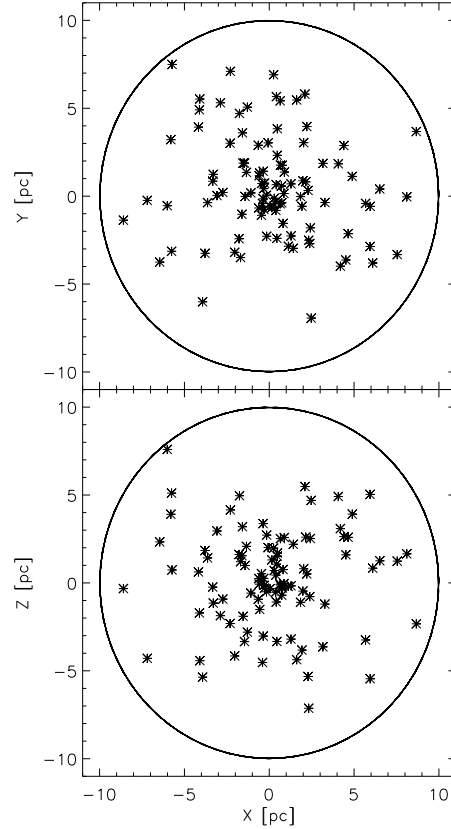
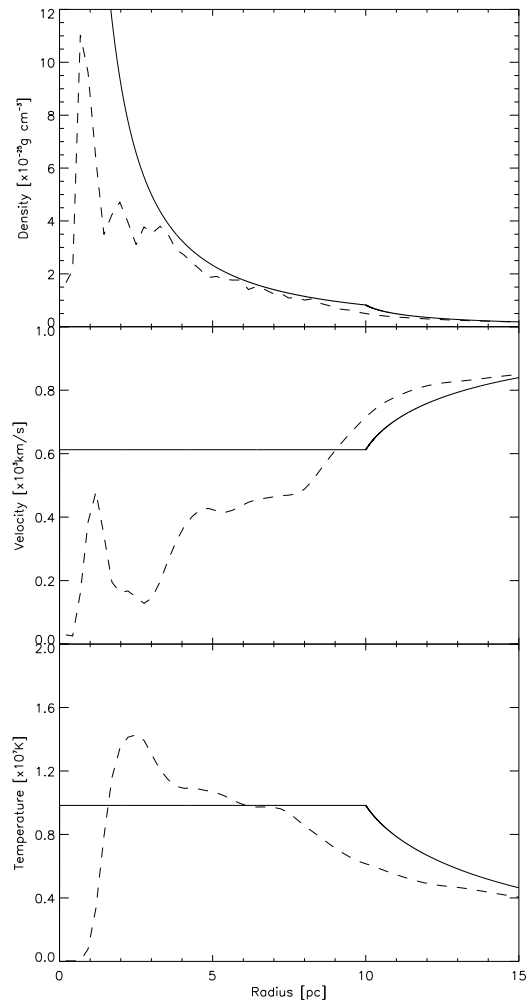
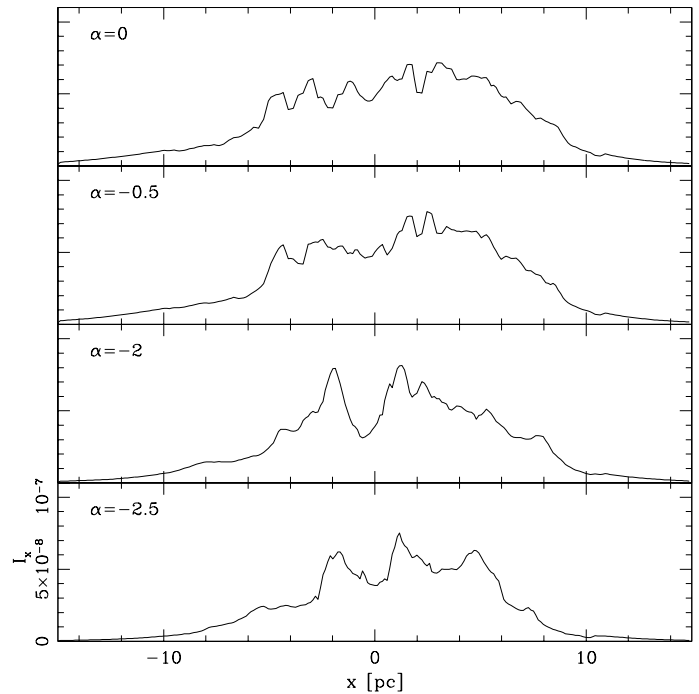


Figure 8. Same as Figure 1 for  $\alpha = -2.5$  model.

- Cantó, J., Raga, A.C. & Rodríguez, L.F., 2000, *ApJ*, 536, 896.  
 Chevalier, R.A. & Clegg, A.W., 1985, *Nature*, 317, 44.  
 Cotera, A.S., Erickson, E.F., Colgan, S.W.J., Simpson, J.P., Allen, D.A. & Burton, M.G., 1996, *ApJ*, 461, 750.  
 Dere, K. P., Landi, E., Young, P. R., & del Zanna, G. 2001, *ApJS*, 134, 331.  
 Dyson, J.E., 1992, *MNRAS*, 255, 460.  
 Gallagher, J. & Smith, L., 1999, *MNRAS*, 304, 540.  
 Hartquist, T.W., Dyson, J.E., Pettini, M. & Smith, L.J., 1986, *MNRAS*, 221, 715.  
 Holtzmann, J.A., Faber, S.M., Shaya, E.J., Lauer, T.R., Groth, J., Hunter, D.A., Baur, W.A., Edwald, S.P., Hester, J.J., Light, R.M., Lynds, C.R., O’Neil, E.J.Jr & Westphal, J.A., 1992, *AJ*, 103, 691.  
 Johnson, K., Leitherer, C., Vacca, W. & Conti, P., 2000, *AJ*, 120, 1273.  
 Lizano, S., Cantó, J., Garay, G. & Hollenbach, D., 1996, *ApJ*, 468, 739.  
 Matvienko, E. E., Shchekinov, Y. A., 2005, *ApJ* 38, 262  
 Melnick, J., Moles, M., & Terlevich, R., 1985, *A&A*, 149, L24.  
 Melo, V.P., Muñoz-Tuñón, C., Maíz-Apellániz, J. & Tenorio-Tagle, G., 2005, *ApJ*, 619, 270.  
 Nagata, T., Woodward, C.E., Shure, M. & Kobayashi, N., 1995, *AJ*, 109, 1676.  
 Raga, A. C., Navarro-González, R., & Villagrán-Muniz, M. 2000, *Revista Mexicana de Astronomía y Astrofísica*, 36, 67.



**Figure 9.** Same as Figure 2 for  $\alpha = -2.5$  model.



**Figure 11.** X-rays  $z = 0$  emission profiles for a line of sight at  $x, y = 0$  for the four x-rays maps in Figure 10.

This paper has been typeset from a  $\text{\TeX}/\text{\LaTeX}$  file prepared by the author.

Raga, A.C., Velazquez, P.F., Cantó, J., Masciadri, E. & Rodríguez, L.F., 2001, *ApJ*, 559, L33.

Rockefeller, G., Fryer, C. L., Melia, F., Wang, Q. D., 2005, *ApJ*, 623, 171.

Raga, A. C., de Gouveia Dal Pino, E. M., Noriega-Crespo, A., Mininni, P. D., & Velázquez, P. F. 2002, *A & A*, 392, 267.

Serabyn, E., Shupe, D. & Figer, D.F., 1998, *Nature*, 394, 448.

Silich, S., Tenorio-Tagle, G. & Rodríguez-González, A., 2004, *ApJ*, 610, 226.

Strickland, D. & Stevens, S., 2000, *MNRAS*, 314, 511.

Walcher, C. J., Böker, T., Charlot, S., Ho, L. C., Rix, H.-W., Rossa, J., Shields, J. C., & van der Marel, R. P. 2006, *ApJ*, 649, 692.

Whitmore, B.C. & Schwizer, F. 1995, *AJ*, 109, 960.

Whitmore, B. C. 2001, *Astrophysical Ages and Times Scales*, 245, 411.

Yusef-Zadeh, F., Law, C., Wardle, M., Wang, Q. D., Fruscione, A., Lang, C. C. & Cotera, A., 2002, *ApJ*, 570, 665.